Jinhang Wu , Ching Tai Ng, Han Fang

Internal damages detection for structural timber members using low-frequency anti-symmetric guided wave

Construction and Building Materials, 2022; 322:126355-1-126355-12

Final publication at: http://dx.doi.org/10.1016/j.conbuildmat.2022.126355

Journal article:

Jinhang Wu, Ching Tai Ng, Han Fang. (2022). Internal damages detection for structural timber members using low-frequency anti-symmetric guided wave. Construction and Building Materials 322:126355.

Internal Damages Detection for Structural Timber Members Using Low-frequency Anti-symmetric Guided Wave

Jinhang Wu, Ching Tai Ng*, Han Fang
School of Civil, Environmental & Mining Engineering, The University of Adelaide, SA 5005, Australia

Abstract

Structural timber is one of the commonly used construction materials. Timber can contain natural internal defect such as knot or natural decay due to its anatomical complexity. Moreover, internal damage or stiffness reduction can also be induced by environmental and biological factors such as weathering and termite attacks. This hidden internal damage increases the difficulty of damage detection using conventional non-destructive testing (NDT) methods. Ultrasonic guided wave (GW) damage detection technique is one of the promising damage detection techniques, which can be employed to achieve an effective and robust damage inspection in timber. However, limited attention has been paid to the use of GW for damage detection in timber, due to the material anisotropy and inhomogeneity. This paper assesses the capability of GW in detecting different sizes of the internal damages in a structural red oak timber using the fundamental anti-symmetric mode (A_0) of GW. Measured GW signals in forward and backward scattering directions are used to calculate the reflection and transmission ratios for different sizes of internal damages. A series of comprehensive experimental and numerical parametric studies are carried out using three-dimensional (3D) finite element (FE) simulations. Good agreement is obtained between numerical and experimental results. The experimentally verified FE model is utilized to further investigate the wave reflection and transmission phenomena from different characteristics of internal damages, such as different lengths, widths, thicknesses, and through thickness locations. The outcomes of this study demonstrate the robustness of GW technique in detecting conspicuous internal damages in structural timber. It demonstrates the feasibility of quantitative assessments of internal damage in timber using A_0 GW.

Keywords: Timber; damage assessment; internal defect; Lamb wave; finite element; scattering.

* Corresponding author email: alex.ng@adelaide.edu.au

1. Introduction

1.1. Backgrounds

Timber has been widely utilised in civil construction due to its sustainable and renewable nature [1, 2]. Recent developments in non-destructive testing (NDT) and structural health monitoring (SHM) techniques have enabled a higher standard for damage detection and structural integrity monitoring in structural members made by timber [3-5]. Visual inspection is implemented for timber damage evaluation, but it is incapable of identifying the internal decay or invisible damage [6]. Timber is a natural grow material, it can contain internal defects such as knot, cracks or natural decay. Physical process on either standing trees or onboard timber members can also produce internal defects [6, 7]. Consequently, internal defects usually exist and can affect the structural performance of timber structures. Apart from the natural defects, internal damages can also be induced by working and environmental conditions. This involves cracks generated from the mechanical loadings, interior deterioration from high moisture content (MC) [12] and reduction of bearing capacity from ultraviolet (UV) aging [13]. Moreover, timber structures, especially historical constructions [8], are susceptible to insect attack due to its organic and biomass nature. The internal flaws can be generated by termites and beetles with only small surface entry larvae boreholes, which are hard to be detected by visual inspection [9, 10]. The reduction in timber material for a structural member due to the internal damage can reduce the stiffness of the structure. Mori et al [11] measured and reported a noteworthy diminution in timber Young's modulus and bending strength from artificial holes on timber.

To minimize the risk of failures due to deterioration of structural performance of timber and ensure the structural safety, an effective NDT damage detection method of critical damage at its early-stage is essential. Compared to metallic materials, such as aluminium and steel, mechanical behaviour derivations of timber are more complicated due to its anisotropy, inhomogeneity and presence of natural defects. Hence, different damage detection techniques for timber have been developed and investigated in the literatures and they are described in the following sections.

1.2. Traditional timber damage detection methods

Traditional semi-destructive testing (SDT) methods, such as Resistograph [14, 15] measures the resistance or properties variation of a timber section by means of electric drilling. However, destructive testing is prohibited for most of the modern or preserved historical construction. NDT methods allow evaluating the condition of structures without inducing any damages. Traditional timber damage detection methods have acoustic emissions, vibration-based methods, sounding and conventional ultrasonic methods, such as C-Scan. The effectiveness of a damage detection method to detect the damages depends not only its sensitivity to damage, but also the operational feasibility considering the realistic environmental conditions.

Acoustic emissions [16] is a passive monitoring approach, through which the elastic wave is generated by a sudden redistribution of stress from localized damages rather an external excitation source. Consequently, the location of acoustic energy source can be determined. Vibration based method [17, 18] primarily examines dynamic responses, such as modal frequencies and modeshapes of structures to determine changes in global stiffness of structures [19]. This method can detect the existence of large discontinuities or damages in timber members. However, compared to conventional ultrasonic method, vibration-based method is less sensitive to small size of damages and incapable of accurately identifying the location of these small damages [19]. Sounding techniques were utilized to measure the embedded length or examine the heath stage of timber utility pole [20]. However, the sonic wave is usually created by means of by impact hammer and belongs to broadband signal. Compared to narrowband signal, broadband excitation signal has higher attenuation and is more dispersive, which is difficult to analyse the signals. On the other hand, the conventional ultrasonic method, such as C-Scan, was also commonly used for damage detection of structural timbers [21]. This method relies on ultrasonic device to generate bulk wave, which was used in detecting small holes [22, 23] and delamination [24] in timber. In the literature, different studies showed it has adequate sensitivity to the damages. However, conventional bulk wave method has limited inspection area: only a small scanning area covered by the ultrasonic device can be inspected. In summary, these techniques are incapable to effectively detect relatively small-size damages. Therefore, a robust method to detect early-stage inconspicuous defects in timber is essential.

1.3. Damage detection of timber structures using guided wave

Guided wave (GW) technique can provide large area inspection and has high sensitivity to different types of damage, thus it has the potential to fulfil the requirements of damage detection for timber. This technique has been widely applied in concrete, metallic and composites materials in the literature [25, 26]. However, limited attention has been paid on damage detection of timber using GW.

In the literature, most of the studies focused on GW and timber were aimed at identifying properties of timber material. Dahmen et al [27] determined nine anisotropic constants of timber using a method combining GWs and bulk waves. The results showed that the computational cost to include all the timber anisotropies is very high. A number of studies indicate that GW is capable of detecting the changes in material properties brought by the environmental factors such as the changes in MCs [28, 29] and UV aging [13]. Fathi et al [28] recently measured the elastic properties of timber under different MC using GW propagation method. They showed that the elastic properties determined using GW are in good agreement with the results obtained from a three-points-bending test. GW has also been recently used to measure the moisture-dependent viscoelastic properties of timber, such as shear storage, shear loss and loss factor [29]. These studies indicate GW can provide a more accurate estimation of the material properties under the changes of MC and UV aging compared to the conventional bulk wave methods.

However, there were limited studies focusing on damage detection of timber members using GW. One of the main real applications of GW technique in timber is to measure the embedded length [3, 30] or to assess the health conditions of timber utility poles [20, 31]. Dackermann et al [20] proposed a new method for monitoring the structural health of timber utility poles. The method combines the machine learning algorisms with GW technique using a multi-sensor system. El Najjar et al [3] assessed the embedded length and the damage in the embedded portions of the timber poles using GW propagation method. They concluded that the wave energy leakage to the surrounding soil is minimal. Numerical studies were also been performed to simulate the wave propagation on the timber poles. Studies showed that timber can be assumed as transversely isotropic material in modelling wave propagating on a timber pole [32, 33]. This is because the stiffness in fibre direction is much greater than the stiffness in the other two directions direction [34]. This assumption was proven to be valid when treating the timber pole as one-dimensional (1D) waveguide. Zhang et al [35] also conducted a preliminary study on damage detection of timber using a piezoelectric transducer (PZT). The wavelet packet energy of GW is calculated for cracks with different lengths.

GW technique has the potential to enable a robust damage inspection in timber, however, limited studies were presented in the literature. Past studies were mainly focused on using GW to measure the timber properties, and only few studies focused on timber damage detection. Therefore, development of GW technique in timber damage detection, typically those inconspicuous internal damages from interior deterioration or insect attack, are remained critical. To the best of author's knowledge, limited studies have provided quantitative assessments on internal damages in structural timber.

This paper aims to provide a comprehensive wave scattering analysis on the internal damage in structural timber member using fundamental anti-symmetric mode (A_0) GW. To assess the sensitivity of A_0 GW to the timber internal damage, different sizes of internal damage have been created experimentally on a structural timber member using a rotary tool. Wave reflection and transmission ratios are obtained before and after the internal damages. In order to have a visual understanding and gain insight into the interaction between the internal damage and the GW, three-dimensional (3D) finite element (FE) simulations are used to model the internal damage. A series of parametric studies using experimentally verified FE model are performed to investigate the wave reflection and transmission ratios by varying the length, width, thickness and location of the internal damages.

The arrangement of the paper is as follows. Section 2 presents the theory of GW propagation in the transversely isotropic timber. Section 3 describes the details of the 3D FE model. Section 4 describes the setup and the procedures in the experiment to create different sizes of internal damages. The reflection and transmission ratios obtained from numerical and experimental results, along with the numerical case studies using the validated FE, are discussed in Section 5. The limitations of the present study are discussed in Section 6. Finally, a conclusion is provided in Section 7.

2. Governing equations for GW propagating in transversely isotropic material

This section presents the governing equations of the GW propagation in timber. Plane wave assumption is used in the analytical solution. Timber is an orthotropic material with elastic properties being different along three principal axes as shown in FIG. 1. Fibre direction is labelled as 1 while tangential and radial direction are labelled as 2 and 3, respectively. The propagation direction of the plane wave is defined to be consistent to the fibre direction 1. Due to the presence of unidirectional fibres, elastic modulus presents large differences between fibre direction and radial direction while only minor difference between radial and tangential direction [32]. Therefore, timber can be assumed to be transversely isotropic material [32, 34].

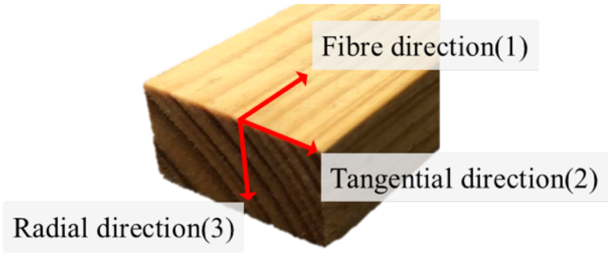

FIG. 1 Three principal axes used in the timber modelling

Governing equations for GWs propagating in an orthotropic plate is given in [36]. For plate wave propagation in a transversely isotropic plate, governing equations can be derived by simply substituting the restrictions on elastic constants to the existing solutions. The compliance matrix of transversely isotropic material can by expressed by taking the inverse of the stiffness matrix as shown in Eq. (1a), where ε and σ are strain tensor and stress tensor, respectively. Five independent variables are required to compute the matrix and they are $E_1, E_3, \vartheta_{13}, \vartheta_{23}$ and G_{13}, where E, ϑ and G are young's modulus, Poisson's ratio and shear modulus in the given direction, correspondingly. ϑ_{ij} and ϑ_{ji} are related by $\frac{\vartheta_{ij}}{E_i} = \frac{\vartheta_{ji}}{E_j}$. Due to directions 2 and 3 have the same material elasticity, a symmetric plane is defined for direction 2-3. Therefore, transverse isotropy has $E_2 = E_3$, $\vartheta_{21} = \vartheta_{31}$ and $G_{12} = G_{13}$, which yields the following simplified symmetric matrix.

$$\varepsilon_{kl} = {c_{ijkl}}^{-1}\sigma_{ij} = \begin{vmatrix} \frac{1}{E_1} & -\frac{\vartheta_{13}}{E_1} & -\frac{\vartheta_{13}}{E_1} & 0 & 0 & 0 \\ -\frac{\vartheta_{13}}{E_1} & \frac{1}{E_3} & -\frac{\vartheta_{32}}{E_3} & 0 & 0 & 0 \\ -\frac{\vartheta_{13}}{E_1} & -\frac{\vartheta_{32}}{E_3} & \frac{1}{E_3} & 0 & 0 & 0 \\ 0 & 0 & 0 & \frac{1}{G_{23}} & 0 & 0 \\ 0 & 0 & 0 & 0 & \frac{1}{G_{13}} & 0 \\ 0 & 0 & 0 & 0 & 0 & \frac{1}{G_{13}} \end{vmatrix} \begin{pmatrix} \sigma_{11} \\ \sigma_{22} \\ \sigma_{33} \\ \sigma_{23} \\ \sigma_{13} \\ \sigma_{12} \end{pmatrix}, \qquad i,j,k,l = 1,2,3 \text{ (1a)}$$

$$G_{23} = \frac{E_3}{2(1+\vartheta_{23})} \tag{1b}$$

Substituting the stress-strain relationship in Eq. (1) into equations of motion in Eq. (2), coupled displacement equations in three directions can be obtained and shown in Eq. (3) [36]. The propagation direction of the plane wave is defined to be consistent with the fibre direction 1, whereas direction 3 is the thickness direction of the timber.

$$\frac{\partial \sigma_{ij}}{\partial x_j} = \rho \frac{\partial^2 u_i}{\partial t^2} \tag{2}$$

$$u_j = U_j e^{i\xi(x_1+\alpha x_3 - ct)}, \qquad j = 1,2,3 \tag{3}$$

where u_i is the displacement component and U_j displacement amplitude of u_j . ξ is wavenumber and c is phase velocity. α is an unknown representing the ratio of x_3 to x_1 wavenumbers. Eq. (3) leads to

$$K_{mn}\,(\alpha) U_n = 0, \quad m,n = 1,2,3 \tag{4}$$

where the coefficient $K_{mn}\,(\alpha)$ is a symmetric matrix, such that $K_{mn} = K_{nm}$. For the transversely isotropic case, coefficient $K_{mn}\,(\alpha)$ are:

$$\begin{aligned} K_{11} &= C_{11} - \rho c^2 + C_{55}\alpha^2 \\ K_{22} &= C_{55} - \rho c^2 + C_{44}\alpha^2 \\ K_{33} &= C_{55} - \rho c^2 + C_{33}\alpha^2 \\ K_{23} &= 0 \\ K_{13} &= (C_{13} + C_{55})\alpha \\ K_{12} &= 0 \end{aligned} \tag{5}$$

where contracted notions are defined and used in Eq. (5) to replace c_{ijkl} in Eq. (1a) with C_{ab} following the order of stress tensor index, consequently: 11 = 1, 22 = 2, 33 = 3, 23 = 4, 13 = 5 and 12 = 6. For consistency of the solutions, $C_{11}, C_{33}, C_{44}, C_{55}$ and C_{13} are chosen to express all coefficient. According to Nayfeh et al [36], shear horizontal mode (SH) are uncoupled mathematically from fundamental symmetric mode (S_0) and A_0 if wave propagates along principle axis in a transversely isotropic plate. Equating determinant of Eq. (4) to zero gives a sixth order polynomial [36]:

$$\alpha^6 + B_1\alpha^4 + B_2\alpha^2 + B_3 = 0 \tag{6}$$

where B_1, B_2 and B_3 are coefficients involving material constants and phase velocity. Both coefficients and solution for α are given in Appendix A.

Solve Eq. (6), substitute α into displacement and stress expressions and apply stress free conditions at plate boundaries [36], the characteristic equations for the symmetric and antisymmetric Lamb wave modes propagate along principal axis in a transversely isotropic plate can be obtained as shown in Eqs. (7)-(9). Eq. 7(a) is for symmetric waves while Eq. 7(b) applies to anti-symmetric waves [36].

$$\frac{\tan(\gamma\alpha_1)}{\tan(\gamma\alpha_3)} = \frac{D_{11}D_{23}}{D_{13}D_{21}} \quad (7a)$$

$$\frac{\tan(\gamma\alpha_1)}{\tan(\gamma\alpha_3)} = \frac{D_{13}D_{21}}{D_{11}D_{23}} \quad (7b)$$

$$\gamma = \frac{\xi d}{2} \quad (8)$$

$$\begin{aligned} D_{1k} &= (C_{13} + C_{33}\alpha_k W_k) \\ D_{2k} &= C_{55}(\alpha_k + W_k) \\ W_k &= \frac{\rho c^2 - C_{11} - C_{55}\alpha_k^2}{(C_{13} + C_{55})\alpha_k} \end{aligned} \quad (9)$$

where d is the thickness of the plate and $k = 1,2,3,4,5,6$.The corresponding roots for α are given in Appendix A. Semi-analytical solutions of Eqs. (7)-(9) are shown in Section 3.1.

3. 3D FE model

3D FE models were developed using ABAQUS/Explicit to simulate the GW propagation and wave scattering phenomena in timber. Reflection and transmission ratios from different sizes of internal damage were obtained. An experiment was performed to validate the FE results. The validated FE model was then used to perform a series of parametric studies, and the results are given in Section 5.

3.1. Model definition

A 10 mm thick Tasmanian red oak was modelled in ABAQUS, which is the same as the specimen used in the experiment. To avoid unwanted reflections from the edges, the width and length of the timber were set to be 800 mm, which are large enough to avoid wave reflections from edges. The configuration of the model is shown in FIG. 2(a). A Cartesian coordinate is established to describe the locations of measurement points. The coordinate is defined at the surface of the timber, and the origin of system is defined at the excitation centre. x direction is aligned with timber fibre direction, which is also the direction of wave propagation. A symmetric boundary condition with respect to x axis was applied. Different sizes of internal damages were created at x = 290mm. To ensure the reflection wave is separated from the incident wave, the reflection wave measurement point is at x = 100mm while the transmission wave measurement point is at equal distance away from the damage with respect to reflection scanning point. The timber is modelled using 3D eight-node linear brick elements with reduced integration and hourglass control (C3D8R) element. To investigate the precision of using reduced integration element, 3D eight-node linear brick elements with incompatible mode, full integration, and hourglass control (C3D8I) were also used to model timber. C3D8I not only utilises full integration but also has additional degree of freedom, which can also capture bending motion. Identical results were obtained from these two models. Since C3D8I is more computationally expensive, C3D8R was used in this study.

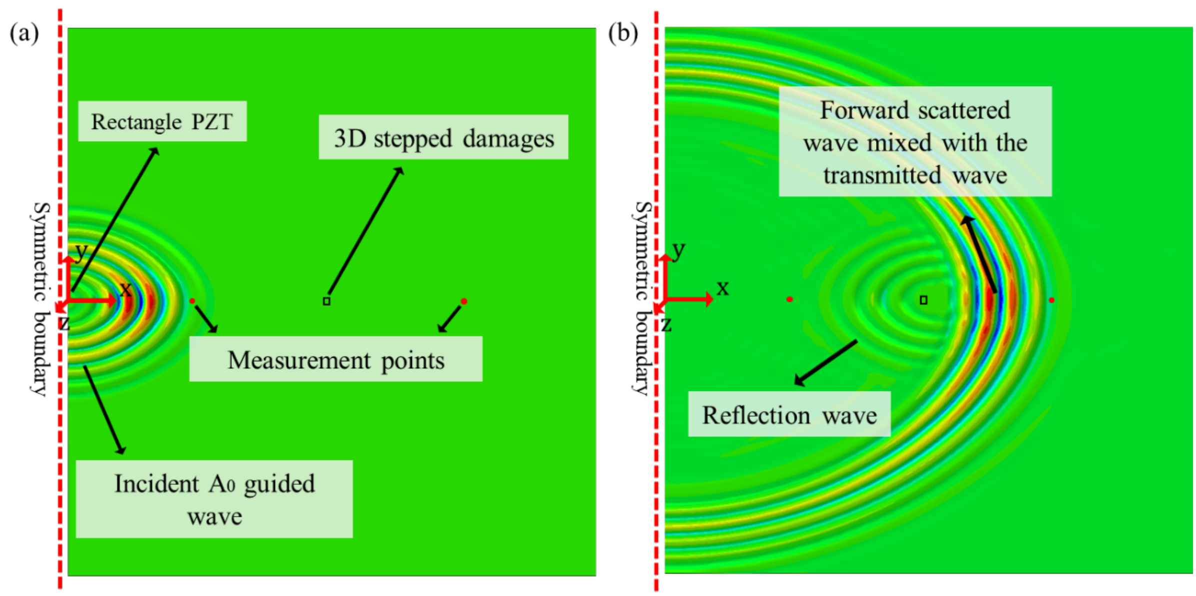

FIG. 2 Screenshot of out-of-plane displacements in *z* axis in a 10 mm red oak at different time steps: (a) right after incident A_0 wave was generated; (b) interaction of A_0 wave with the 3D stepped damages.

Red oak was modelled using transversely isotropic material in this study. The material properties are listed in Table 1 and density of the timber was measured to be 647.7 kg/m^3 [34]. Fibre direction (E_{11}) is aligned with *x* direction as shown FIG. 2. Young's modulus of fibre direction (E_{11}) is measured experimentally by means of time-of flight using GW, which is 10.5 GPa, shared a similar value of 8.91 GPa from reference [34].

Table 1 Elastic properties of Tasmanian red oak

E_{11} (GPa)	E_{22} (GPa)	E_{33} (GPa)	ϑ_{12}	ϑ_{13}	ϑ_{23}	G_{12} (GPa)	G_{13} (GPa)	G_{23} (GPa)
10.50	1.24	1.24	0.05	0.05	0.43	0.89	0.89	0.43

To simulate the wave attenuation in the model, Rayleigh damping is employed to simulate energy dissipation during wave propagation [25]. Attenuation constant k_i represents the rate of energy dissipation along the direction of the wave propagation and it is determined by fitting an exponential function to the experimental data for the decrement of signal amplitude versus distance [37, 38]. Eq. (10) shows the formula to obtain k_i, where x_1 and x_2 are the locations of measurement points, while A_1 and A_2 are the wave amplitudes, correspondingly.

$$\frac{A_1}{A_2} = \exp\left(k_i(x_2 - x_1)\right) \tag{10}$$

Mass-proportional damping constant (α_ω) and stiffness-proportional constant (β_ω) can then be computed using k_i. $\alpha_\omega = 2k_i c_g$ and $\beta_\omega = \frac{\alpha_\omega}{\omega^2}$, where c_g and ω are the group velocity and angular central frequency.

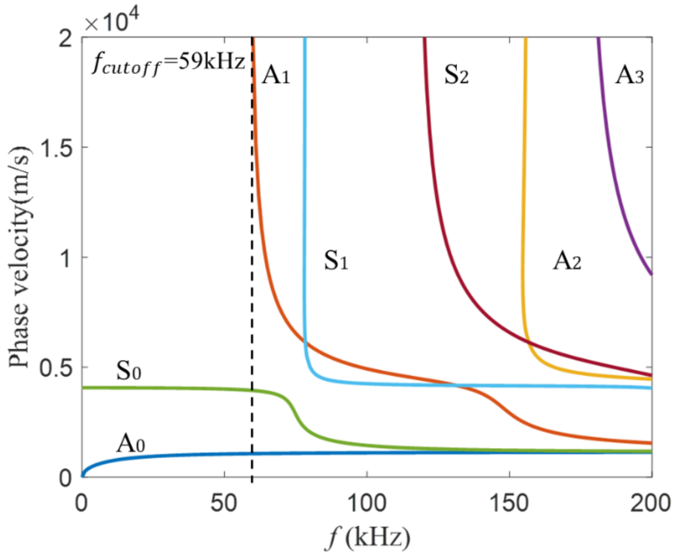

FIG. 3 Dispersion diagram for wave propagation along 0° in x direction in 10 mm Tasmanian red oak

The dispersion relationships for Lamb wave propagating along 0° in x direction in 10 mm Tasmanian red oak can be obtained by solving the governing equations Eqs. (7)-(9). The wave modes for up to 200 kHz are shown in FIG. 3. As shown in the FIG. 3, A_0 wave has smaller phase velocity and wavelength than S_0 GW under same excitation frequency. Therefore, A_0 GW is more sensitive to smaller damages, and hence, it is selected as the excitation wave mode in this study. The cut off frequency is 59 kHz. To minimize the complexity in wave analysis of higher orders and multi-modes, the excitation frequency is chosen below 59kHz. Theoretically, a higher frequency can have a smaller wavelength, which is more sensitive to smaller size of damage. However, it is found that 35 kHz can provide the best signal-to-noise ratio for the experimentally measured signal. Therefore, the excitation signal is selected as a 5-cycle narrow-band 35 kHz Hann windowed pulse and used for the rest of the study.

In the FE simulation, the A_0 wave is generated by applying out-of-plane displacements on a 12 mm × 6 mm rectangle region, which has the same size and shape as the PZT used in the experiment. The maximum element size and time increment were recommended to be less than $\Delta l = \frac{\lambda}{20}$; $\Delta t = \frac{1}{20f}$ to ensure the stability and accuracy of explicit analysis [39], where Δl is the maximum element size, Δt is the time step, λ is the wavelength of excitation signal, and f is the central excitation frequency. The wavelength is 28 mm for A_0 GW under selected excitation frequency 35 kHz. Therefore, the maximum element size is set to be 1 mm to ensures there are at least 28 elements existed per wavelength. To ensure the out-of-plane displacement is accurately modelled, the thickness of the element is set to be 1 mm and there are 10 layers of element in the thickness direction.

FIG. 2 (a) shows a snapshot of out-of-plane displacement in FE right after A_0 GW is excited. As shown in the displacement contour, the energy of incident A_0 wave concentrates along the fibre direction, which has dominant stiffness. Therefore, the measurement locations are defined along fibre direction to capture most of the wave energy. FIG. 2 (b) shows the interaction of A_0 with the internal damage. As a result, reflection wave and forward scattered wave are generated at the damage. It can also be seen that the forward scattered wave is mixed with the transmitted wave.

3.2. Simulation of internal damages

Internal damages were approximated as 3D semi-stepped damages in the model validation. This approximation was developed from a 2D stepped notch damage model, which was simulated to represent corrosion damage in metallic materials [40]. It was found that the stepped notches provide a realistic approximation to the corrosion damage. Therefore, it was utilized and further enhanced to 3D semi-stepped damages to represent the internal damages in the experiment.

Internal damages were created experimentally with a small surface entry, whose diameter equal to D_1. The diameter of the damage gradually increases from D_1 at the surface and reaches a maximum diameter D_2 at the mid-depth $(\frac{d}{2})$ of the timber, where d is the thickness of the timber. A schematic diagram of a 3D semi-stepped damage is shown in FIG. 4. As it can be seen in the x-y plane view, each layer of the 3D semi-stepped damage composed by a square. The diameter of the square damage gradually increases from the top surface (D_1) to mid-plane (D_2). Different internal damage cases were created by enlarging D_2, while D_1 and depth of the damage remained the same in the experiment. However, due to D_1, D_2 and depth of the damage were fixed, an identical 3D stepped damage with "unit increasing step" is inapplicable. For example, when there are n layers of squares, each layer will possess a thickness of $d/2n$ mm. However, the length and width of the squares in each layer are fixed as $(D_2 - D_1) / (2n - 2)$ mm. Therefore, if h/n is not equal to $(D_2 - D_1) / (2n - 2)$, the shape of each "unit step" becomes "semi-stepped". Denser elements were used to mesh the damage region to achieve good elements aspect ratio. Different sizes of 3D semi-stepped damages were validated by the experimental results and shown in Section 5.1. The experimentally validated FE model was then used to perform a series of numerical parametric studies to obtain the reflection and transmission ratios for different internal damage cases in Sections 5.2 and 5.3.

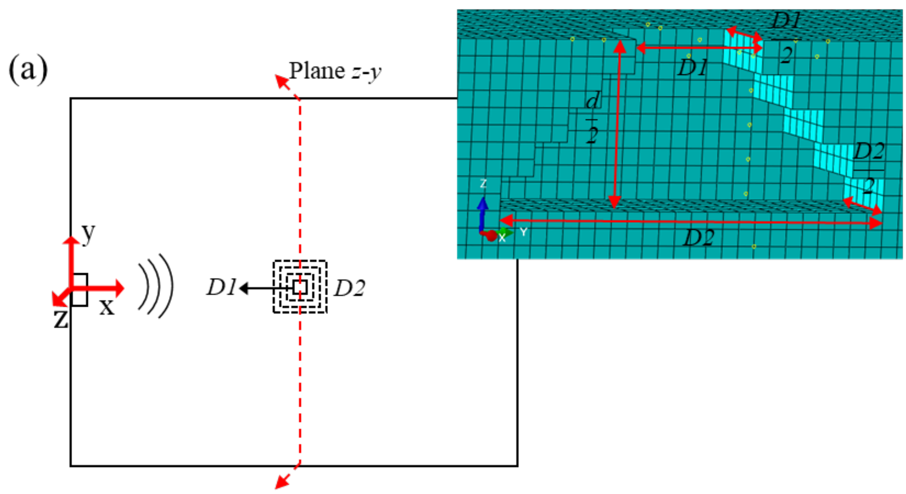

FIG. 4 Schematic diagram for a 3D FE semi-stepped damage

4. Experiment

An experiment was conducted to provide validation of the FE model, and physical understanding of the GW propagation in the timber and scattering at the internal damage. Reflection and transmission waves were measured for different sizes of internal damages to obtain the reflection and transmission ratios. A $10 \times 90 \times 1000$ mm^3 $(d \times w \times l)$ red oak structural timber was used in this study, which has the same thickness as FE model. Red oak is categorized as hard wood, which possesses a stiffer rigidity compared to most softwoods. Specimen dimensions are the same as the original product to ensure the practicability of the experiment. The properties of oak were determined as described in Section 3.1. All experimental measurements were conducted in an indoor environment on the same day. The indoor temperature was maintained at 27°, and hence, the moisture content of timber sample is assumed to remain unchanged. Internal damage generation, and the measurements for reflection and transmission wave are performed on a selected region of the specimen. The timber grain of the region is selected to be smooth, and hence, no natural defects or obvious cracks are presented. Therefore, it is ensured that the received scattering waves are only generated by the internal damage

The A_0 wave was excited by a 2×12×6 mm^3 $(d \times w \times l)$ surface-mounted rectangle PZT. The PZT was placed at 300 mm away from the right end and at the centre of the specimen. The locations of reflection and transmission wave scanning points, and the locations of internal damage are the same as those used in the FE simulation as shown in FIG. 2. The excitation signal was a 5-cycle narrow-band 35 kHz Hann windowed pulse, generated by a NI PXIE-5122 signal module. Due to the narrow width of the specimen, absorbing clay was attached at four edges of the timber to absorb unwanted wave reflections from edges. A Kron-Hite 7500 amplifier was used to amplify signal voltage. Signals were measured by a Polytec 1D scanning laser Doppler vibrometer before and after the wave interaction with the damages [41, 42]. Since the focus of this study is on A_0 GW, only out-of-plane displacements were measured. Reflective paints were evenly sprayed on scanning areas to improve light reflections on sample surface for the measurements. Sampling frequency was set to be 10.24 MHz with 1200 times samples averaging. A photo and a figure of schematic experimental setup are shown in FIG. 5(a).

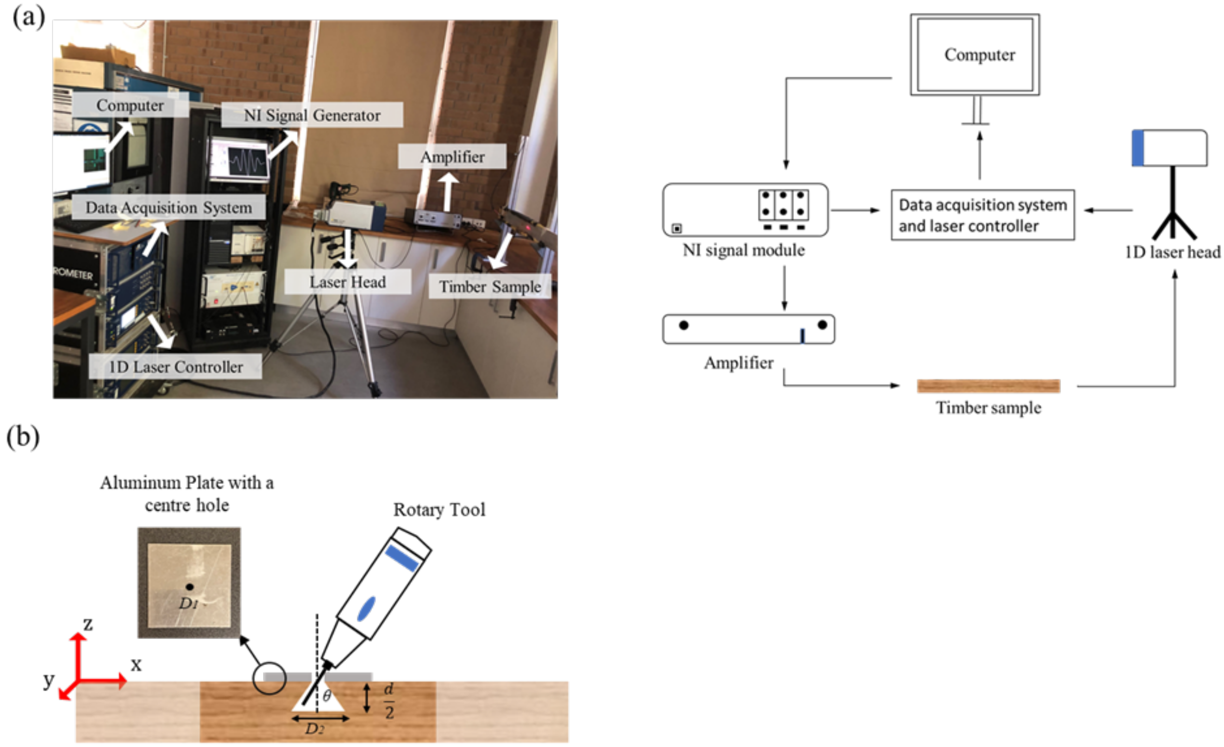

FIG. 5 (a) experimental setup and (b) zoomed view of the sections where internal damages were implemented in experiment

4.1. Experimental validation

Before implementing internal damages on the specimen, the accuracy of the wave simulation in FE was validated by experimental results and the analytical dispersion curve. A 2D discrete Fourier transform (DFT) method was used in this study to validate A_0 GW in both numerical models and experiment results. 2D DFT method transforms the time-domain signals, which acquired from numbers of equally spaced measurement points along wave path, to frequency-wave number domain, so that superimposed wave signal resulting from multi-modes can be separated [43]. Applying 2D DFT to space-time signal $u(x,t)$ yields the following results [43]:

$$H_{\xi+1,f+1} = \frac{1}{MN}\sum_{n=1}^{N}\sum_{m=1}^{M} u_{n,m} e^{-2\pi i(\frac{\xi}{N}(n-1)+\frac{f}{M}(m-1))} \quad (10)$$

where f and ξ donate frequency and wavenumber; $u_{n,m}$ is the space-time signal consisting of M time samples at N measurement points.

Time-domain signals at 60 evenly spaced points along fibre direction were measured on the intact specimen. The excitation wave was a 5-cycle narrow-band 35 kHz Hann windowed pulse, which is the same as the FE model. The same Cartesian coordinate in FIG. 2 is used to describe the measurement locations. The first measurement point is located at x = 100 mm, the rest of the points were distanced by an equal distance of 5 mm. It was experimentally determined that the number of measurement points and an equal measurement spaced of 5 mm are good enough to produce an acceptable resolution in the contour. In addition, zero paddings were used in time-domain and space-domain data to increase resolutions of the plots. Identical measurement locations were also defined in the FE model for performing the 2D DFT.

The 2D DFT results obtained from FE and experiment are shown in FIG. 6 (a) and FIG. 6 (b), respectively. A wavenumber-frequency contour is plotted with the analytical dispersion curves for the 10 mm thick oak timber under the excitation frequency of 35 kHz. As shown in FIG. 6 (a) and (b), there is excellent agreement for the experiment and FE data. The contours have good agreement with analytical A_0 dispersion curves. Moreover, contours reach a maximum amplitude around 35 kHz, which is the centre frequency of the excitation pulse and marked using a blue circle. The results show that A_0 is strongly dominant under the low frequency condition (35 kHz), and S_0 GW is not observed from the contour.

To capture the wave attenuations with FE, the out-of-plane displacements were also measured at the scanning area. By using Eq. (10), Rayleigh damping constants were computed as k_i=1.965 *Np/m*, α_ω= 4677.093 *rad/s* and β_ω = 9.671×10^{-8} *s/rad*.

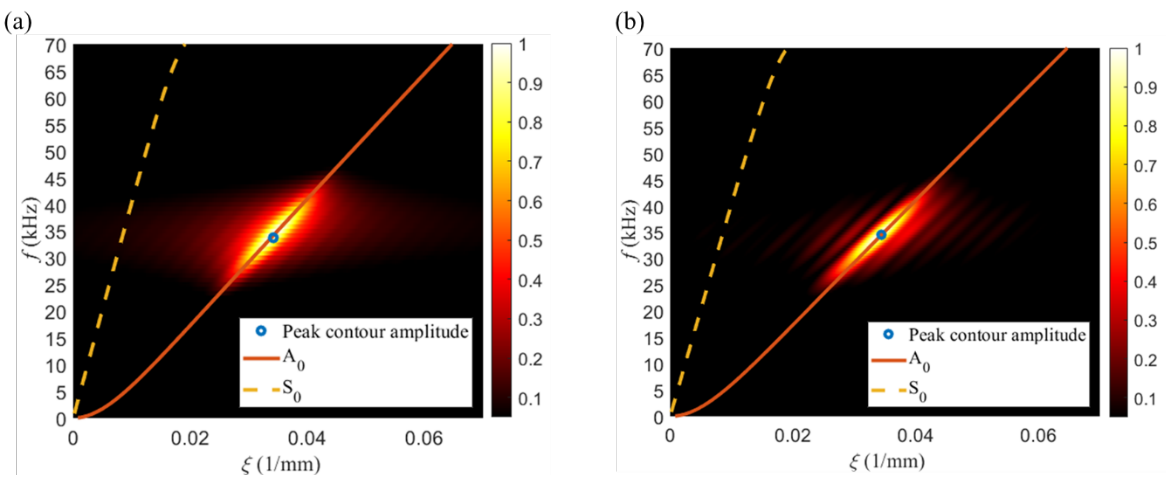

FIG. 6. Wavenumber-frequency contour plot and the analytical dispersion curves (solid line: A_0, S_0: dashed line) for a 10mm thick red oak, (a) FE results (b) Experimental results by 35kHz incident wave.

4.2. Generation of internal damage

Five different sizes of internal damages were investigated to obtain the reflection and transmission wave ratios. The locations of reflection and transmission wave scanning points, and the locations of internal damage are the same as in those used in the FE simulation as shown in FIG. 2.

FIG. 5 (b) shows a schematic diagram of the internal damage implementations. The diagram zooms in on the sections where internal damage is implemented. Experimentally, an internal damage cannot be created without comprising the integrity of the surface of the timber specimen. Therefore, a small surface hole with diameter (D_1 = 6 mm) is created to allow an internal access. The diameter of the internal damage increases gradually from the surface (D_1) and reaches the maximum diameter D_2 at mid-plane ($\frac{d}{2}$ = 5 mm) of the timber using a rotary tool. To control the sizes of internal damage diameters, an aluminium plate with a centre hole (diameter is equal to D_1), was temporarily mount on top of the timber surface. The centre hole on the aluminium plate provides a fixed rotational angle (θ) between rotary head and the vertical line, which provide a reasonable accuracy in generating the D_2 of the damage. To create different sizes of D_2, different sizes of rotary heads were substituted in the rotary tool. Each internal damage was created by rotating the rotary tool in 360°, which was considered to have equal damage extent in fibre and tangential direction. Due to the availability of rotary heads and aforementioned difficulties in control of the sizes D_2, five discrete sizes of D_2 were created (7 mm, 9 mm, 12 mm, 14 mm and 16 mm) providing that the depth of the damage and D_1 remain 5 mm and 6 mm, respectively.

Time signals were recorded for each damage size at the aforementioned locations. In addition, a fan was used to clean the accumulative wood dust inside the damage before the next drilling progression. FIG. 7 (a) and (b) compare the FE results with the experiment time signal at reflection and transmission measurement locations for the case when D_2 = 7 mm. The time domain signals at reflection and transmission points are normalized with respect to the incident wave amplitude at the reflection measurement point. Both figures confirmed that the time of arrivals and the wave amplitudes in experiments are accurately predicted by FE. Mode conversion effect could occur through the interaction between A_0 GW and the internal damage, from which, the in-plane waves could be generated. However, the time domain data was recorded in out-of-plane direction only due to the focus of this study is on A_0 GW. The magnitudes of the resulting in-plane waves are very small and have not been observed in the out-of-plane time domain data in both numerical and experimental data. Minor phase shifts are observed in FIG. 7, and due to following reasons: 1) the presence of local inhomogeneities in timber sample and 2) slight misalignments of damage size or location. It is also noticed there is a small unabsorbed wave component from the first reflection at sample width in FIG. 7(a). The unabsorbed wave component does not interfere with the reflection components from the damage as it can be seen that the two components are clearly separated.

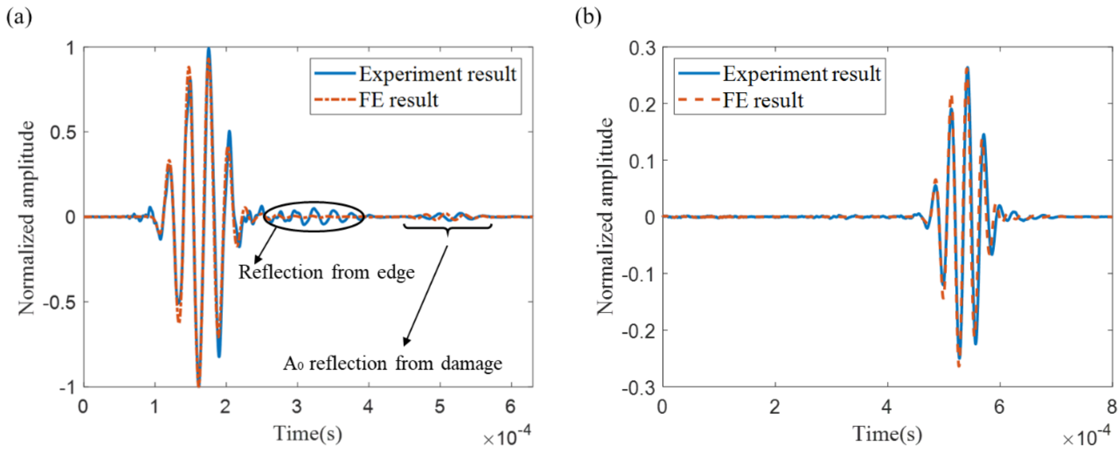

FIG. 7 FE and experimental time signal for internal damage size D_2 = 7 mm at (a) x = 100mm (b) x = 480 mm by 35kHz incident wave

5. Results of numerical case studies

As descripted in Sections 3 and 4, reflection and transmission waves before and after the internal damages were captured. Three ratios are defined to quantify wave reflection and transmission ratios, which are reflection wave ratio r_r, transmission wave ratio r_{tr} and forward scattered wave ratio r_{trb}. These wave pockets are shown in FIG. 2. Forward scattered wave is retrieved by means of baseline subtraction due to it mixes with the transmission wave.

The ratios are calculated based on the same normalization method as before. They are normalized by the areas of the incident wave at the reflection point as follow:

$$r_r = \frac{A_r}{A_i}, \quad r_{tr} = \frac{A_{tr}}{A_i}, \quad r_{trb} = \frac{A_{tr} - A_{udtr}}{A_i} \tag{10}$$

where A_i, A_r and A_{tr} represent the areas under the incident pulse, reflection pulse, and transmission pulse in time-domain signal, respectively. The time-domain signals were computed as the absolute values when used to calculate the areas under the signal. A_{udtr} represents the areas under transmission wave for the undamaged case. As aforementioned, it is used for the purpose of baseline subtraction to obtain the forward scattered wave ratio (r_{trb}).

r_r and r_{tr} from the experimental and numerical results are shown in Section 5.1. The experimentally validated 3D FE model was then used to perform a series of parametric studies to further investigate the reflection and transmission effects from different internal damage cases. The wave measurement locations were defined consistently as before, and the wave excitation frequency was the same as 35 kHz. Section 5.2 shows the effects of internal damages with different dimensions. Section 5.3 shows the effects of the through thickness locations of internal damages.

5.1. Experimental results

r_r and r_{tr} obtained from five different sizes of internal damages are shown in FIG. 8(a) and (b). As for r_{trb}, baseline subtraction is impractical to measure in the experiment. It is because the specimen needs to be taken off from the laser scanning frame for creating the damage, hence, large phase shifts can be induced from a minor change in measurement location or a minor delay in wave generation each time. In general, the experimental results exhibit consistent trends as the FE results. Both experimental and FE results show that the r_r increases with the sizes of D_2 and reaches a peak at D_2 =16 mm, while the r_{tr} presents the opposite trend. A small discrepancy between FE and experiment predictions is observed in both figures. This is due to minor mismatches of shapes and sizes of the internal damages. From FIG. 8, the size of D_2 can be estimated from the reflection and transmission area ratio. Despite the internal damages in the reality have irregular shapes, the experimental results still indicate the great sensitivity and potentials of GW for detecting timber internal damages.

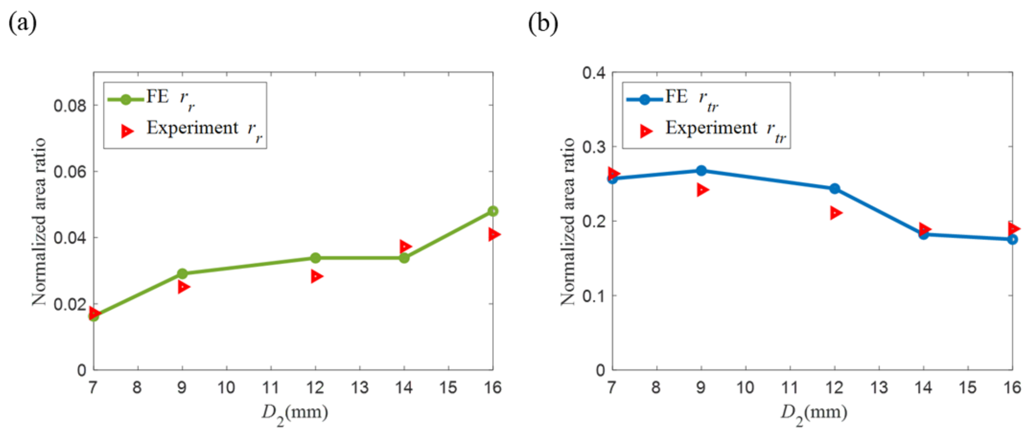

FIG. 8 Normalized area ratio for the (a) reflection wave (b) transmission wave resulting from internal damages by 35kHz incident wave

5.2. Effects of internal damages with different dimensions

The experimentally verified FE model was used to further investigate the reflection and transmission ratios for varying length (*l*), width (*w*), and thickness (*t*) of the internal damage. As shown in FIG. 9, the internal damages were modelled in an ideal cuboid shape to quantify *l*, *w* and *t* of the damage. The centroid of the internal damage is located at the mid-plane of the timber and is axial symmetric in both plane *x*-*y* and plane *y*-*z*.

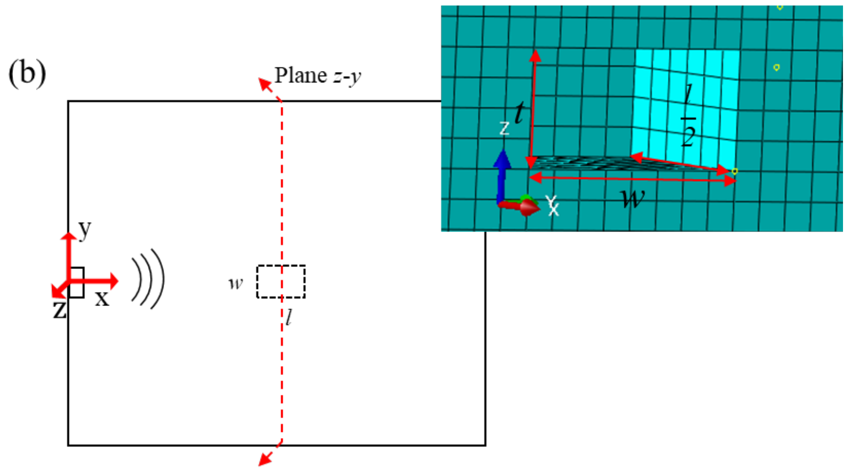

FIG. 9 Schematic diagram for FE internal damage with different dimensions

l and *w* of the damage were quantified with respect to wavelength (λ), while *t* of the damage was quantified with respect to the thickness (d = 10 mm) of the timber. The dimensions of the damage were initialized by 0.2λ×0.2λ×0.2d ($l \times w \times t$). Parametric studies were performed to vary one of these three parameters l, w and t, and keep the other parameters unchanged in the initial stage. l and w of the damage were swept from zero to 2λ with a step of 0.2λ respectively. t of the damage was swept from zero to a hundred percent of the d with a step of 0.1d. The parametric results are presented in the sequence of varying *l*, *w* and *t* as shown in the following paragraphs. In addition to r_r and r_{tr}, r_{trb} is also calculated. This is due to an ideal undamaged baseline is available from the numerical model.

FIG. 10 shows the results for varying *l*. In summary, $r_{tr}$and r_{trb} presented a more intuitive linear increasing trend compared to the r_r. This is due to r_r is affected by the interference between the first reflection pulse from the start of the damage and second reflection pulse from the far end of the damage. Two reflection pulses can either interfere constructively and destructively when length to wavelength ratio is equal to 0.2 and 0.3, respective, as shown in

FIG. 11(a) and FIG. 11(b). A clear separation of two reflection waves can be observed when length to wavelength ratio is equal to 1.8 as shown in FIG. 11(c).

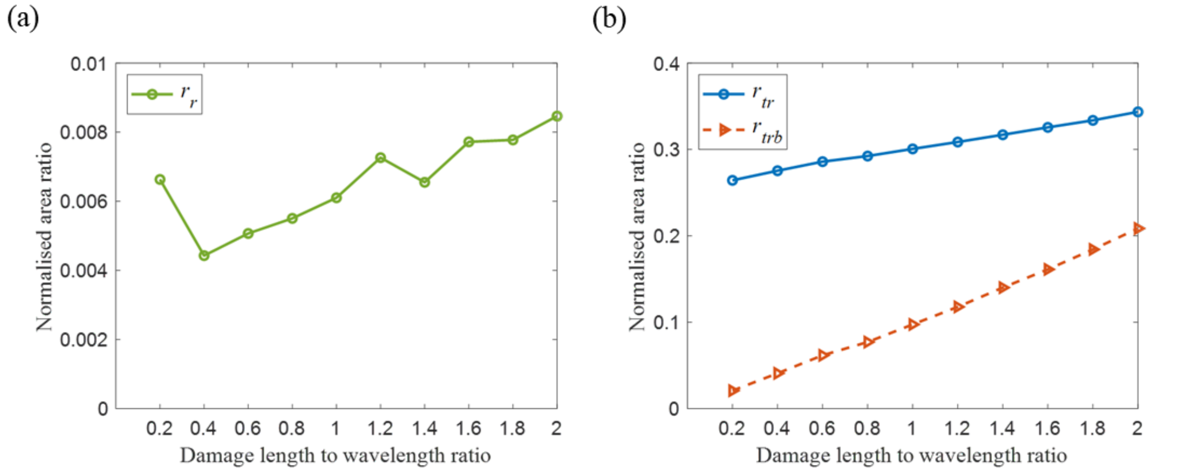

FIG. 10 Normalized area ratio for varying damage length for the (a) reflection wave (b) transmission wave (solid line) and forward scattering wave (dashed line) by 35kHz incident wave

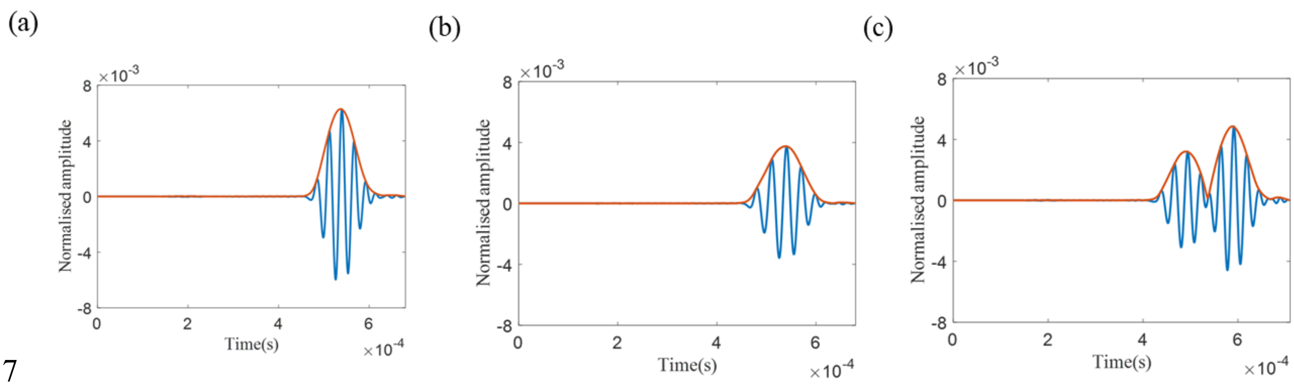

FIG. 11 Time signal of reflection wave at damage length to wavelength ratio equals to (a) 0.2, (b) 0.3 and (c) 1.8 by 35kHz incident wave

FIG. 12 and FIG. 13 show the reflection and transmission results for varying w and t of the damage. As aforementioned, the l of the damage was kept to 0.2 wavelength, which minimize the destructive interference effects from interference phenomenon between two reflection waves as shown in FIG. 11(a). Despite the width and thickness of the damage were quantified differently, i.e. width was quantified with respect to wavelength while thickness was to the thickness of the timber, the trends of r_r, r_{tr} and r_{trb} in both cases display almost identical patterns. The results clearly indicate that r_r increases monotonically with the increasing damage width and depth, while r_{tr} and r_{trb} experienced a slight fluctuation.

In summary, r_r shows a more intuitive increasing pattern for the increasing size of internal damage compared to r_{tr} and r_{trb} and therefore more suitable to be used for identifying the increasing size of the internal damage. Despite in general, r_{tr} and r_{trb} have larger amplitude than r_r, it is found that the patterns of r_{tr} and r_{trb} can fluctuate for different damage cases. Moreover, the measurement of the transmission wave requires the additional access to the far end of the damage, and hence, it is less practical compared to the measurement of the reflection wave.

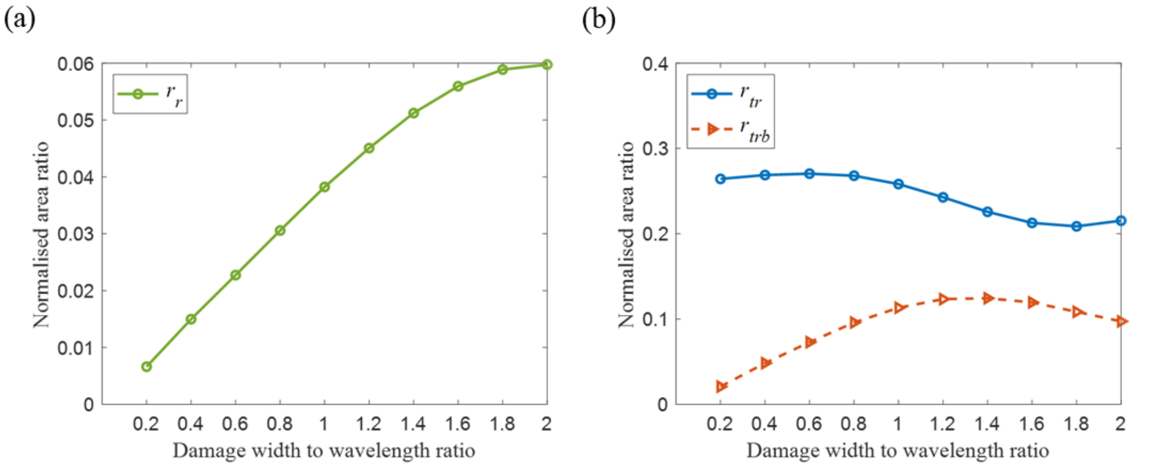

FIG. 12 Normalized area ratio for varying damage width for the (a) reflection wave (b) transmission wave (solid line) and forward scattering wave (dashed line) by 35kHz incident wave

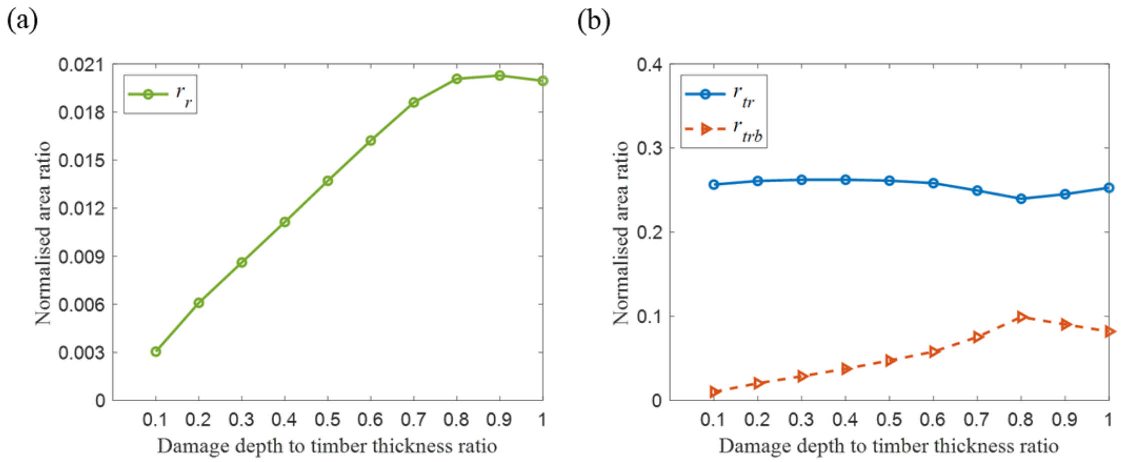

FIG. 13 Normalized area ratio for varying damage thickness for the (a) reflection wave (b) transmission wave (solid line) and forward scattering wave (dashed line) by 35kHz incident wave

5.3. Effect of internal damages with different thickness locations

Section 5.2 shows that results of the reflection and transmission wave for varying *l*, *w* and *t* are different. On the other hand, internal damage can exist in any through thickness locations. Therefore, it is also important to investigate the sensitivity of A_0 GW to the through thickness locations of the internal damage. Internal damages with different though thickness locations were modelled by the experimentally validated FE model. The FE model and wave excitation frequency are the same as those used as Section 5.2. FIG. 14 shows a schematic diagram of the through thickness locations of the damage. The dimensions of the damage are 0.2λ×2λ×0.1d ($l \times w \times t$). The through thickness locations of the damage is represented by the lower surface of the damage and described by z axis. Therefore, the locations of the damage were moved from upper surface z = -1 mm to z = -10 mm with a step of 0.1d. It is noteworthy that when z = -1 mm and z = -10 mm, the damage is a surface notch located at the upper and the lower surface of the timber, respectively.

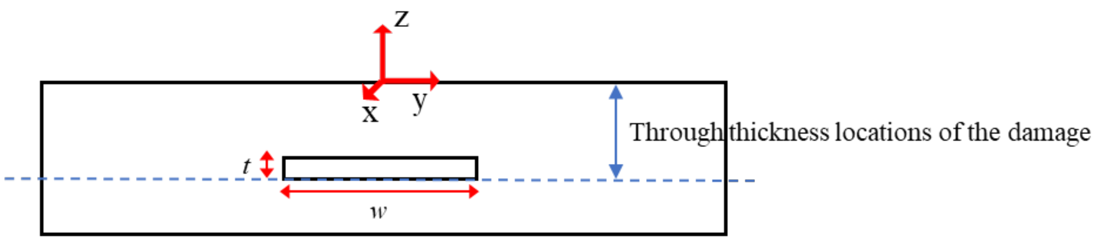

FIG. 14 Schematic diagram of through thickness location of the internal damage

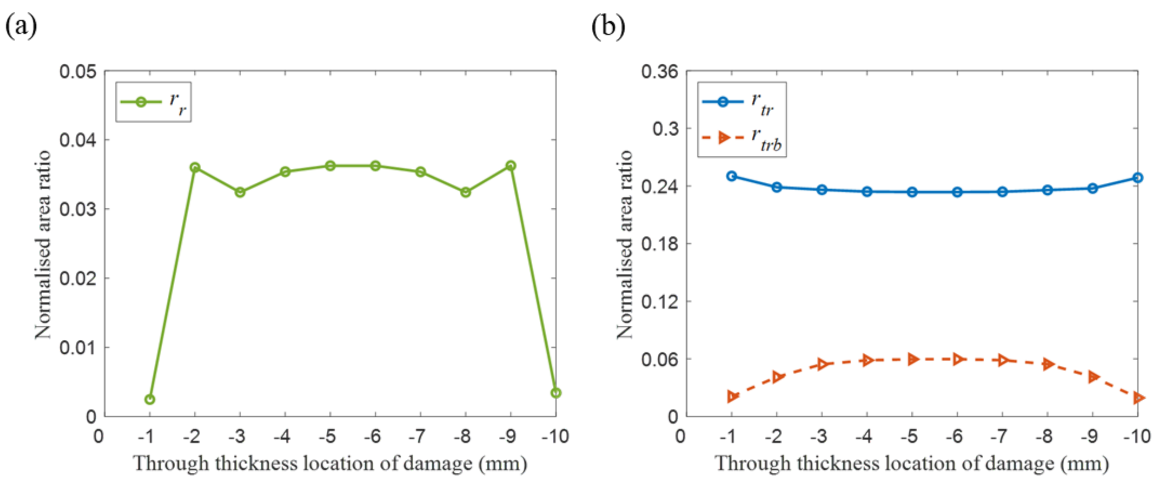

FIG. 15 Normalized area ratio for internal damage with different through thickness locations (lower surface of the damage in z axis location) for the (a) reflection wave (b)

transmission wave (solid line) and forward scattering wave (dashed line) by 35kHz incident wave

The reflection and transmission results are shown in FIG. 15(a) and (b). r_r, r_{tr} and r_{trb} show symmetric patterns with respect to the mid-plane of the timber. This is because of the symmetric out-of-plane displacement mode shape of A_0. The changes of the damage location can change the bending stiffness of the timber. Therefore, the response of reflection wave r_r changes correspondingly. According to FIG. 15(a), r_r reached the maximum amplitude of at the mid-plane of the timber at *z* = -5 mm and *z* = -6 mm, while r_r has the minimum amplitude at the damage is a surface notch at *z* = -1 mm and *z* = -10 mm. It is also noteworthy that when the damage is a surface notch, z = -1 mm and *z* = -10 mm, the amplitude of r_r is much smaller than that is located internally. Therefore, based on the amplitude of r_r, it is concluded that A_0 GW is more sensitive to the damage located internally than the damage located at the surface i.e. surface notch at 35 kHz. Furthermore, the fluctuation of r_r also indicated that even if the damage size is the same, the reduction in timber stiffness can vary for the different through thickness locations of the damage.

6. Limitations of the proposed study

Despite the reflection and transmission area ratios measured from the experimental internal damages display a simple monotonical pattern, the application of GW for practical application in timber damage detection can be more complex. The limitations of the proposed methods are discussed in this section.

The first challenge is the multimodal nature of GW. As shown in FIG. 3, the cut-off frequency for a 10mm red oak timber is 59kHz. To minimize the complexity in wave analysis of higher orders and multi-modes, the excitation frequency is chosen below the cut-off frequency. In real-cases, timber might have a much larger thickness than the specimen in this study. This results a smaller cut-off frequency and therefore the excitation frequency needs to be reduced. For structural timber with large thicknesses, a different GW type such as surface wave, longitudinal wave might be considered as the excitation mode. Moreover, the generation of internal damage and the measurements for reflection and transmission wave are performed on a selected region of the specimen in this study. The wood grain of the region is selected to be smooth, and hence, no natural defects or obvious cracks are presented. When the size of timber is much larger, it is impossible to avoid the existence of timber natural defects. Therefore, a baseline state of the sample with natural defects is required to extract the damage-related information, which can become a more complex analysis. To account for the high-variability in damage conditions and timber properties, the GW technique can be combined with the data-driven approaches such as machined learning in future research, which paves the way for real-cases online monitoring.

7. Conclusion

This paper has provided a comprehensive wave scattering study from the internal damages for a structural timber using GW. The study helps to improve the in-situ timber damage assessment using GW. Different sizes of internal damage have been created experimentally on a structural timber member using a rotary tool. The reflection and transmission ratios of wave have been measured before and after the internal damages. The experimental internal damages have been modelled by the 3D semi-stepped damage in 3D FE simulation. A good agreement has been achieved between the experimental and the numerical results. In summary, both r_r and r_{tr} obtained from the experiment results have simple trend, in which r_r increases with the size of the damage while r_{tr} has the opposite trend. Therefore, it can be used for identifying the internal damage size in the experiment. To simplify the level of anisotropy, timber properties have been modelled as transversely isotropic for simulating the wave propagation on the timber, and have proven to be accurate in the FE simulation. It has been shown that the energy of the wave concentrates along the fibre direction and the low frequency incident A_0 GW has low attenuation when propagating along the fibre direction.

The experimentally validated FE model was used to study the reflection and transmission effects of damages with different l, w and t. In general, r_r presents an intuitive increasing pattern compared to r_{tr} and r_{trb} and therefore more suitable to be used for identifying the increasing size of the internal damage. However, the amplitude of r_r is smaller than the r_{tr} in most of the cases. It has also been observed that when varying l of the damage, two reflection waves from start and far end of the damage can either interfere constructively, or destructively due to different arrival times of the two reflection waves. Therefore, a slight fluctuation has been observed in r_r for varying the damage l. In addition, the reflection and transmission effects of damage with different though thickness locations have been studied. It has been found that for the same size of damage, when the location of the damage is at the surface, i.e., a surface notch, the amplitude of r_r is much smaller than those cases when the damage is located internally.

In summary, this study has confirmed the robustness and sensitivity in detecting conspicuous damages in timber using A_0 GW. The findings in this study have provided improved insights into GW interaction with internal damage in structural timber, revealing the potentials for the application of GW in timber damage detection.

8. Acknowledgement

This work was funded by the Australian Research Council (ARC) under the grant number DP210103307. The authors are grateful for this support.

9. References

1. Ghanbari-Ghazijahani, T., J. Wu, and C.-T. Ng, *Plastic buckling and axial crushing of concrete-filled steel tubes: usage of multiple wood blocks.* Thin-Walled Structures, 2020. **150**: p. 106487.
2. Palma, P. and R. Steiger, *Structural health monitoring of timber structures - Review of available methods and case studies.* Construction and Building Materials, 2020. **248**: p. 118528.
3. El Najjar, J. and S. Mustapha, *Condition assessment of timber utility poles using ultrasonic guided waves.* Construction and Building Materials, 2021. **272**: p. 121902.
4. Aseem, A. and C.T. Ng, *Debonding detection in rebar-reinforced concrete structures using second harmonic generation of longitudinal guided wave.* NDT & E International, 2021. **122**: p. 102496.
5. Pineda Allen, J.C. and C.T. Ng, *Nonlinear Guided-Wave Mixing for Condition Monitoring of Bolted Joints.* Sensors, 2021. **21**(15): p. 5093.
6. Ross, R.J., *Inspection of timber bridges using stress wave timing nondestructive evaluation tools: a guide for use and interpretation*. Vol. 114. 1999: US Department of Agriculture, Forest Service, Forest Products Laboratory.
7. Mousavi, M., et al., *Feature extraction of wood-hole defects using empirical mode decomposition of ultrasonic signals.* NDT & E International, 2020: p. 102282.
8. Cruz, H., et al., *Guidelines for on-site assessment of historic timber structures.* International Journal of Architectural Heritage, 2015. **9**(3): p. 277-289.
9. Hadlington, P.W., *Australian termites and other common timber pests*. 1996: UNSW Press.
10. Ghaly, A. and S. Edwards, *Termite damage to buildings: Nature of attacks and preventive construction methods.* Am J Eng Appl Sci, 2011. **4**(2): p. 187-200.
11. Mori, M., et al., *Nondestructive evaluation of bending strength of wood with artificial holes by employing air-coupled ultrasonics.* Construction and Building Materials, 2016. **110**: p. 24-31.

12. Dietsch, P., et al., *Methods to determine wood moisture content and their applicability in monitoring concepts.* Journal of Civil Structural Health Monitoring, 2015. **5**(2): p. 115-127.
13. Nasir, V., H. Fathi, and S. Kazemirad, *Combined machine learning–wave propagation approach for monitoring timber mechanical properties under UV aging.* Structural Health Monitoring, 2021: p. 1475921721995987.
14. Kappel, R. and C. Mattheck, *Inspection of timber construction by measuring drilling resistance using Resistograph F300-S.* WIT Transactions on the Built Environment, 2003. **66**.
15. Ceraldi, C., V. Mormone, and E.R. Ermolli, *Resistographic inspection of ancient timber structures for the evaluation of mechanical characteristics.* Materials and structures, 2001. **34**(1): p. 59-64.
16. Diakhate, M., et al., *Cluster analysis of acoustic emission activity within wood material: Towards a real-time monitoring of crack tip propagation.* Engineering Fracture Mechanics, 2017. **180**: p. 254-267.
17. Yang, X., et al., *Application of modal analysis by transfer function to nondestructive testing of wood I: determination of localized defects in wood by the shape of the flexural vibration wave.* Journal of wood science, 2002. **48**(4): p. 283-288.
18. Hu, C. and M.T. Afzal, *A statistical algorithm for comparing mode shapes of vibration testing before and after damage in timbers.* Journal of Wood Science, 2006. **52**(4): p. 348-352.
19. Farrar, C.R., S.W. Doebling, and D.A. Nix, *Vibration–based structural damage identification.* Philosophical Transactions of the Royal Society of London. Series A: Mathematical, Physical and Engineering Sciences, 2001. **359**(1778): p. 131-149.
20. Dackermann, U., B. Skinner, and J. Li, *Guided wave–based condition assessment of in situ timber utility poles using machine learning algorithms.* Structural Health Monitoring, 2014. **13**(4): p. 374-388.
21. Ross, R.J., B.K. Brashaw, and R.F. Pellerin, *Nondestructive evaluation of wood.* Forest products journal, 1998. **48**(1): p. 14.
22. Mousavi, M., et al., *Feature extraction of wood-hole defects using empirical mode decomposition of ultrasonic signals.* NDT & E International, 2020. **114**: p. 102282.
23. Yang, H. and L. Yu, *Feature extraction of wood-hole defects using wavelet-based ultrasonic testing.* Journal of forestry research, 2017. **28**(2): p. 395-402.
24. Sanabria, S.J., et al., *Air-coupled ultrasound inspection of glued laminated timber.* 2011.
25. Soleimanpour, R. and C.-T. Ng, *Scattering analysis of nonlinear Lamb waves at delaminations in composite laminates.* Journal of Vibration and Control, 2021: p. 1077546321990145.
26. Hu, X., C.T. Ng, and A. Kotousov, *Scattering characteristics of quasi-Scholte waves at blind holes in metallic plates with one side exposed to water.* NDT & E International, 2021. **117**: p. 102379.
27. Dahmen, S., et al., *Elastic constants measurement of anisotropic Olivier wood plates using air-coupled transducers generated Lamb wave and ultrasonic bulk wave.* Ultrasonics, 2010. **50**(4-5): p. 502-507.
28. Fathi, H., S. Kazemirad, and V. Nasir, *Lamb wave propagation method for nondestructive characterization of the elastic properties of wood.* Applied Acoustics. **171**: p. 107565.
29. Fathi, H., S. Kazemirad, and V. Nasir, *A nondestructive guided wave propagation method for the characterization of moisture-dependent viscoelastic properties of wood materials.* Materials and Structures, 2020. **53**(6): p. 1-14.

30. Li, J., M. Subhani, and B. Samali, *Determination of embedment depth of timber poles and piles using wavelet transform.* Advances in Structural Engineering, 2012. **15**(5): p. 759-770.
31. Yu, Y., et al., *Wavelet packet energy–based damage identification of wood utility poles using support vector machine multi-classifier and evidence theory.* Structural Health Monitoring, 2019. **18**(1): p. 123-142.
32. Subhani, M., J.C. Li, and B. Samali, *A comparative study of guided wave propagation in timber poles with isotropic and transversely isotropic material models.* Journal of Civil Structural Health Monitoring, 2013. **3**(2): p. 65-79.
33. Subhani, M., et al., *Reducing the effect of wave dispersion in a timber pole based on transversely isotropic material modelling.* Construction and Building Materials, 2016. **102**: p. 985-998.
34. Green, D.W., J.E. Winandy, and D.E. Kretschmann, *Mechanical properties of wood.* Wood handbook: wood as an engineering material. Madison, WI: USDA Forest Service, Forest Products Laboratory, 1999. General technical report FPL; GTR-113: Pages 4.1-4.45, 1999. **113**.
35. Zhang, J., Y. Huang, and Y. Zheng, *A feasibility study on timber damage detection using piezoceramic-transducer-enabled active sensing.* Sensors, 2018. **18**(5): p. 1563.
36. Nayfeh, A.H. and D.E. Chimenti, *Free wave propagation in plates of general anisotropic media.* 1989.
37. Ramadas, C., et al., *Modelling of attenuation of Lamb waves using Rayleigh damping: Numerical and experimental studies.* Composite Structures, 2011. **93**(8): p. 2020-2025.
38. Mohseni, H. and C.T. Ng, *Rayleigh wave propagation and scattering characteristics at debondings in fibre-reinforced polymer-retrofitted concrete structures.* Structural Health Monitoring-an International Journal, 2019. **18**(1): p. 303-317.
39. He, S., C.T. Ng, and C. Yeung, *Time-Domain Spectral Finite Element Method for Modeling Second Harmonic Generation of Guided Waves Induced by Material, Geometric and Contact Nonlinearities in Beams.* International Journal of Structural Stability and Dynamics, 2020. **20**(10).
40. Demma, A., et al., *The reflection of guided waves from notches in pipes: a guide for interpreting corrosion measurements.* Ndt & E International, 2004. **37**(3): p. 167-180.
41. Hughes, J.M., et al., *Damage detection with the fundamental mode of edge waves.* Structural Health Monitoring, 2021. **20**(1): p. 74-83.
42. Hughes, J.M., et al., *The fundamental ultrasonic edge wave mode: Propagation characteristics and potential for distant damage detection.* Ultrasonics, 2021. **114**: p. 106369.
43. Alleyne, D. and P. Cawley, *A two-dimensional Fourier transform method for the measurement of propagating multimode signals.* The Journal of the Acoustical Society of America, 1991. **89**(3): p. 1159-1168.

10. Appendix A

Coefficients of Eq. (6) for wave propagates in a transversely isotropic plate

$$B_1 = [C_{11}C_{33}C_{44} - {C_{13}}^2 C_{44} - 2C_{13}C_{44}C_{55} + C_{33}{C_{55}}^2 - (C_{33}C_{44} + C_{33}C_{55} + C_{44}C_{55})\,\rho c^2]/(C_{33}C_{44}C_{55}) \qquad (A1)$$

$$B_2 = [C_{11}C_{33}C_{66} + C_{11}C_{44}C_{55} + {C_{13}}^2C_{55} - 2C_{13}{C_{55}}^2$$
$$- \left(C_{33}C_{11} + C_{11}C_{44} - {C_{13}}^2 - 2C_{13}C_{55} + C_{33}C_{55} + C_{55}C_{44} + {C_{55}}^2\right)\rho c^2$$
$$+ (C_{33} + C_{44} + C_{55})\rho^2 c^4]/(C_{33}C_{44}C_{55}) \qquad (A2)$$

$$B_3 = [C_{11}{C_{55}}^2 - \left(2C_{11}C_{55} + {C_{55}}^2\right)\rho c^2 + (C_{11} + 2C_{55})\rho^2 c^4 - \rho^3 c^6]/(C_{33}C_{44}C_{55}) \qquad (A3)$$

Solutions of Eq. (6) for wave propagates in a transversely isotropic plate

$$\alpha_{1,3} = \frac{-B \pm [B^2 - 4AC]^{\frac{1}{2}}}{2A}, \alpha_2 = -\alpha_1, \alpha_4 = -\alpha_3, \alpha_5 = -\alpha_6 = [(\rho c^2 - C_{66})/C_{44}]^{1/2} \qquad (A4)$$

where

$$A = C_{33}C_{55}$$
$$B = (C_{11} - \rho c^2)C_{33} - (C_{55} - \rho c^2)C_{55} - (C_{13} + C_{55})^2 \qquad (A5)$$
$$C = (C_{11} - \rho c^2)(C_{55} - \rho c^2)$$